Article

Near-Equiatomic μ Phase in Self-Sharpening Tungsten-Based High-Entropy Alloys

Tian-Wei Liu [1,2]**, Tong Li** [1,2] **and Lan-Hong Dai** [1,2,]*

1   State Key Laboratory of Nonlinear Mechanics, Institute of Mechanics, Chinese Academy of Sciences, Beijing 100190, China; liutianwei@lnm.imech.ac.cn (T.-W.L.); litong@imech.ac.cn (T.L.)
2   School of Engineering Science, University of Chinese Academy of Sciences, Beijing 100049, China
*   Correspondence: lhdai@lnm.imech.ac.cn

Abstract: The topologically close-packed (TCP) μ phase is usually known as an undesirable precipitation in highly alloyed Ni-base superalloys and steels. However, the ultrastrong μ phase with micron/nano-scale distribution plays a key role in driving the emergence of self-sharpening in our recently developed WMoFeNi high-entropy alloy (HEA). Herein, a detailed study is carried out to understand the substructure and atomic occupation of the μ phase by scanning electron microscope (SEM) and aberration-corrected transmission electron microscope (ACTEM). The Fe/Ni and W/Mo element pairs are equivalent in the μ-phase structure. Moreover, the elements in μ phase exhibit a near-equiatomic ratio, and the μ phase can grow during annealing at 1150 °C. $(0001)_μ$ and $(1\bar{1}02)_μ$ Twins are the main substructures of the μ phase, and their atomic configurations and twinning mechanisms are investigated. The geometrical structural analysis of μ phase possesses a great significance for the design of self-sharpening HEAs.

Keywords: high-entropy alloys; TCP phase; μ phase; self-sharpening; transmission electron microscope

1. Introduction

Tungsten and other refractory element alloys possess excellent mechanical and physical properties, such as high melting point, high density, high hardness, and superior high-temperature strength [1–3]. Therefore, they are usually utilized in high-temperature alloys and widely used in kinetic energy penetrators, radiation shields, and rocket nozzles in spacecraft [3–5]. High entropy alloys (HEA), which provide a new design concept of material development, have garnered significant research attention due to a wide range of component designs [6,7]. Based on elemental composition, HEAs possess a controllable structure and excellent performance, such as high-temperature stability, low-temperature toughness, and superior corrosion resistance [8–14]. Combined with the design concept of HEAs and properties of W alloys, some refractory HEAs, such as WMoNbTa and WMoNbVTa, have been developed [15–20].

When W, Co or other refractory elements are combined with Ni or Fe, topologically close-packed (TCP) phases are inevitably produced, which form the largest group of intermetallic compounds with complex structures, such as in Ni superalloys, steels, and high-entropy alloys (HEAs) [21–25]. In previous studies [21–29], it has been reported that the precipitation of TCP phases seriously deteriorates the mechanical properties of alloys. Among various TCP phases, μ phase commonly forms in alloys with a high content of Co or W [26–29] and plays a crucial role in performance improvement. The brittleness of μ phase is one major obstacle that hinders widespread applications, originating from its complex and dense stacking structure. Though the TCP μ phase is usually considered as an undesirable precipitate phase in alloys [26–32], it is found in our recent study that the μ phase has an important application prospect for self-sharpening in multi-phase tungsten-based HEA (W-HEA) [33]. The excellent self-sharpening is revealed to be triggered by

the ultrastrong μ phase stimulated high strain gradient and dynamic recrystallization softening [33–38]. To better understand the effect of TCP μ phase on shear susceptibility, the deformation mechanism of μ phase should be unveiled, which is also critical for performance improvement. The deformation mechanism of TCP μ phase in Ni-base superalloys and other alloys has been widely studied [26–32]; however, there are few studies related to the substructure of μ phase in HEAs.

Herein, the near-equiatomic TCP μ phase substructures are investigated in multi-phase WMoFeNi HEA by X-ray diffraction (XRD), scanning electron microscope (SEM), and transmission electron microscopy (TEM). In general, the μ phase grows during annealing and high-density twins are formed on the basal and cylindrical planes. The Fe/Ni and W/Mo elemental pairs are equivalent and replace each other in the occupied position of the μ phase. In addition, structural defects and substructures are studied using atomic-resolution HAADF-STEM images and geometrical analysis, providing insights into the deformation mechanism of the μ phases. Furthermore, the influence of μ phase particles on the formation of shear bands is discussed. The study of μ phase with substructures and particles-associated shear susceptibility provides guidance for the design of self-sharpening HEAs.

2. Experimental Procedure

The equiatomic WMoFeNi HEA (W-HEA) ingot was prepared by arc melting equimolar mixtures of corresponding pure metals (purity > 99.9 wt. %). High-purity Ti was used as a getter for residual gases in a high-purity argon atmosphere. The ingot was re-melted and flipped more than five times to eliminate chemical inhomogeneities, the detailed fabricated process can be found in reference [33]. Then, small plates with the size of about 10 mm × 10 mm × 1.5 mm were spark-cut from the ingot. Some specimens were annealed at 1150 °C for 24 h and then quenched into ice water. The microstructural characterization and compositional analysis were performed using an FEI Quanta 200 FEG SEM, equipped with an energy dispersive X-ray spectrometer (FEI Inc., Hillsboro, OR, USA). Phase identification was carried out by XRD (Rigaku SMARTLAB diffractometer, Rigaku Inc., Tokyo, Japan), equipped with Cu Kα radiations and operated at 45 kV–200 mA. The diffraction patterns were collected in the 2θ range of 25° to 90° at the scan rate of 2°/min.

The transmission electron microscopy (TEM) specimen was prepared by mechanical grinding and polishing to a thickness of 50–70 μm, which was then subjected to twin-jet electro-polishing and finally ion-milled at room temperature with Gatan PIPS II 695 C (GATAN Inc., Pleasanton, CA, USA). The microstructural observations were conducted using JEM 2100F (JEOL Inc., Tokyo, Japan) with an operating voltage of 200 kV. The atomic-resolution HAADF-STEM analysis was conducted using an FEI Titan 80-300 (FEI Inc., Hillsboro, OR, USA), operating at 300 kV.

3. Results and Discussion

The phase composition, mechanical properties, morphology, and elemental composition of the as-cast and annealed W-HEA specimens are shown in Figure 1. The alloy comprises three phases based on the XRD results (Figure 1a). The fracture strength of as-cast and annealed specimens can reach 1510 MPa and 1390 MPa, respectively (Figure 1b). Furthermore, the elemental composition of three phases before and after annealing is shown in Figure 1c,d. Figure 1c shows SEM image of the as-cast specimen, clearly demonstrating the presence of three phase structures. The dark-grey matrix phase possesses a face-centered cubic (FCC) structure (marked as B, Fe-Ni-rich phase), where the bright-white large dendrites dispersed in the matrix possess a body-centered cubic (BCC) structure (marked as A, W-Mo-rich phase). Some small particles dispersed in the FCC matrix or located at the interface of FCC and BCC correspond to the μ phase (marked as C). Figure 1d shows an SEM image of the specimen annealed at 1150 °C for 24 h and quenched into ice water. The phase structure is obviously changed in the annealed specimen. The μ phase grows further (especially at the interface between FCC and BCC phases), whereas the relative proportions

of FCC and BCC phases decrease significantly. Figure 1c shows that W is found in the BCC phase, while Fe and Ni are found in FCC and μ phases. Moreover, Mo exhibits a relatively obvious distribution in the μ phase. After annealing at 1150 °C (Figure 1d), there is almost no change in the chemical composition of FCC and BCC phases. However, many W atoms diffuse into the μ phase and result in a near-equiatomic ratio of four constituent elements (Figure 1c,d). The compositional data are summarized in Table 1. The atomic distribution at atomic scale of Fe, Ni, W, and Mo is detected by aberration-corrected scanning transmission electron microscopy (ACTEM) using the HAADF-STEM model (Figure 1e–h). In addition, the Fe/Ni (red-colored spheres) and W/Mo (blue-colored spheres) pairs are equivalent in the μ structure, occupying two kinds of atomic positions (Figure 1i).
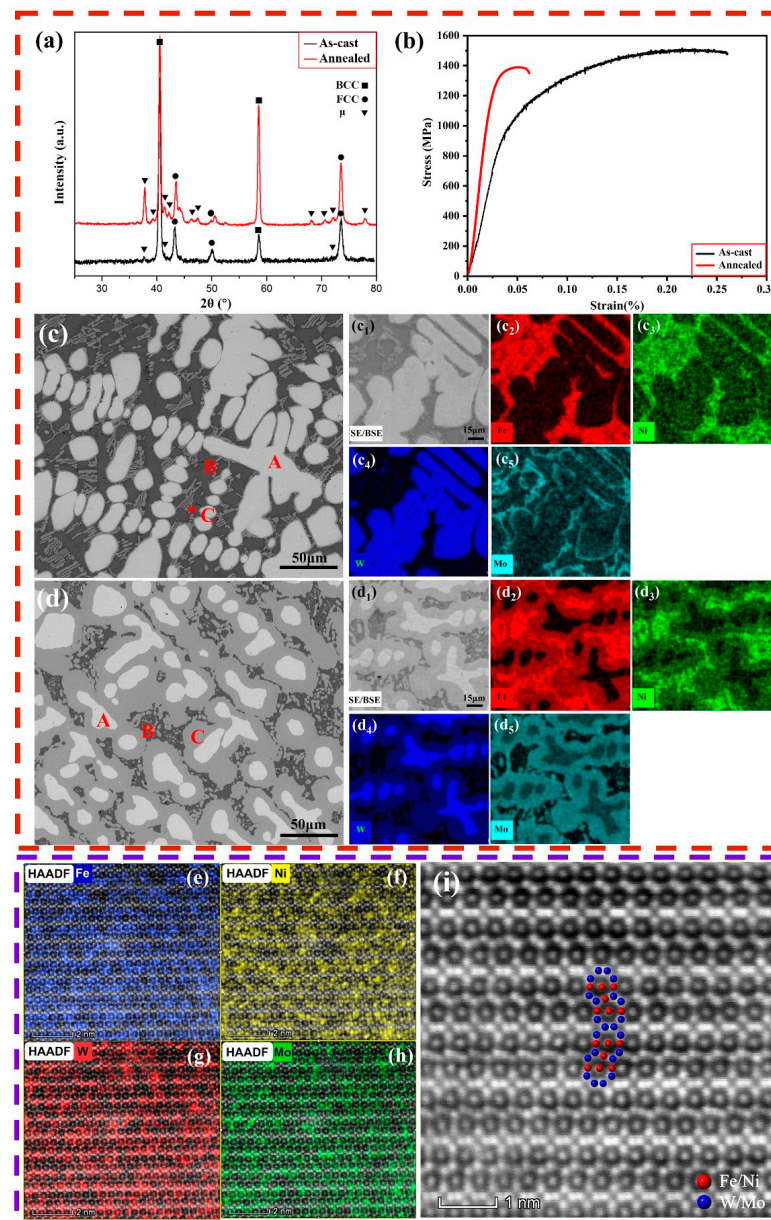

Figure 1. (**a**) XRD patterns of the as-cast and annealed specimens; (**b**) stress–strain curves of the as-cast and annealed specimens; (**c**) SEM image of the as-cast specimen, where (**c$_1$**–**c$_5$**) show the morphology and elemental distribution of the as-cast specimen; (**d**) SEM image of the specimen after annealing at 1150 °C for 24 h, whereas (**d$_1$**–**d$_5$**) show the morphology and elemental distribution of the annealed specimen; (**e**–**h**) EDS maps of the μ phase for Fe, Ni, W, and Mo elements using STEM; and (**i**) STEM lattice image of the μ phase.

Table 1. The composition of three phases in HEA.

Phase	Material State	Chemical Compositions (at. %)			
		Mo	Fe	Ni	W
Total		24.6 ± 1.4	24.4 ± 1.0	24.0 ± 0.6	27.0 ± 0.8
A (BCC)	As-cast	31.1 ± 1.9	3.7 ± 0.3	2.3 ± 0.3	62.9 ± 2.0
	Annealed	31.1 ± 2.2	3.5 ± 0.5	1.3 ± 0.5	64.2 ± 2.2
B (FCC)	As-cast	13.6 ± 1.1	40.7 ± 1.3	40.5 ± 2.0	5.2 ± 2.0
	Annealed	9.2 ± 2.0	37.4 ± 1.5	49.4 ± 1.6	3.9 ± 2.1
C (μ phase)	As-cast	33.1 ± 2.8	33.9 ± 2.1	22.9 ± 1.0	10.1 ± 1.5
	Annealed	27.7 ± 2.3	28.9 ± 2.3	22.3 ± 1.7	21.1 ± 2.4

3.1. Characterization of the μ Phase

In XRD patterns (Figure 1a), except for FCC and BCC diffraction peaks, the diffraction peaks of μ phase becomes clearer after annealing at 1150 °C for 24 h, which corresponds to the increase in mass fraction of μ phase in the specimen. The μ phase, which is based on the A_7B_6 stoichiometry, has a rhombohedral crystal structure (space group 166, R$\bar{3}$m) [26–32] and the lattice parameters of the μ phase are $a = b = 0.475$ nm, $c = 2.567$ nm. Moreover, the rhombohedral unit cell of the μ phase is given in Figure 2a. Moreover, detailed TEM observations were carried out to further study the structure of μ phase. Figure 2b shows a bright-field TEM image of the as-cast W-HEA specimen, where some μ phase particles are dispersed in the FCC matrix and the size of μ phase is hundreds of nanometers in diameter. Figure 2c,d presents corresponding selected area electron diffraction (SAED) patterns, which are taken from the white-colored circled region "*c*" in Figure 2b by tilting. Figure 2e shows the SAED pattern taken from the white-colored circled region "*e*" in Figure 2b.
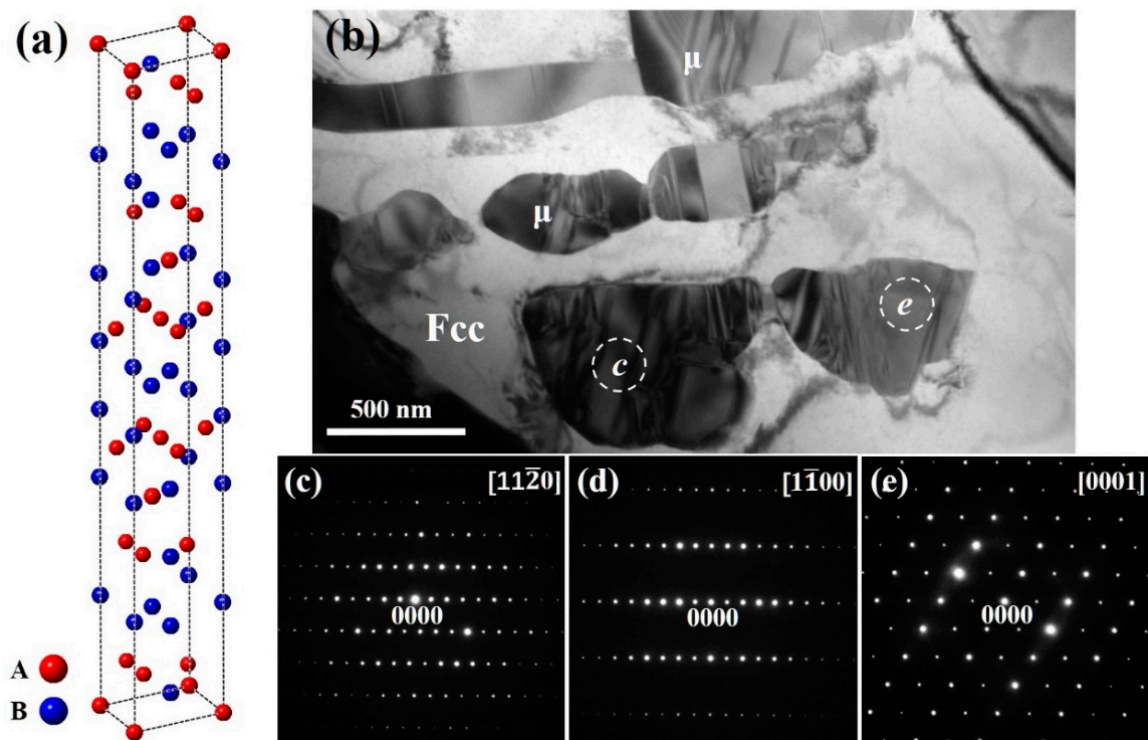

Figure 2. (**a**) Unit cell of the μ phase, (**b**) a bright-field TEM image of the μ phase, (**c**,**d**) corresponding SAED patterns of the μ phase using in situ tilting from the region "*c*" in (**b**), corresponding to a tilt angle of 30° from (**c**) to (**d**), and (**e**) corresponding SAED pattern from the cycled region "*e*" in (**b**).

From Figure 2b, a large number of stacking faults (SFs) and twins' contrast can be seen in the μ phase. The crystal structure of μ phase can be described as an alternative stacking of the Zr_4Al_3 and $MgCu_2$ units [28–31]. Moreover, the units are stacked parallel to the $(0001)_\mu$ basal plane. The basal slip of dislocations is a basic deformation mechanism in μ phase, which is accomplished by synchro-shear inside Laves triple-layers [28,30]. In previous studies, three kinds of basal plane faults were observed in the μ phase [26–28,30]. Except for the basal faults, $(\bar{1}101)_\mu$ and $(1\bar{1}02)_\mu$ pyramidal plane faults were also investigated [26–28]. In this study, the basal slip and $(1\bar{1}02)_\mu$ pyramidal slips are observed. The detailed substructural observations of the μ phase are shown in Figure 3.
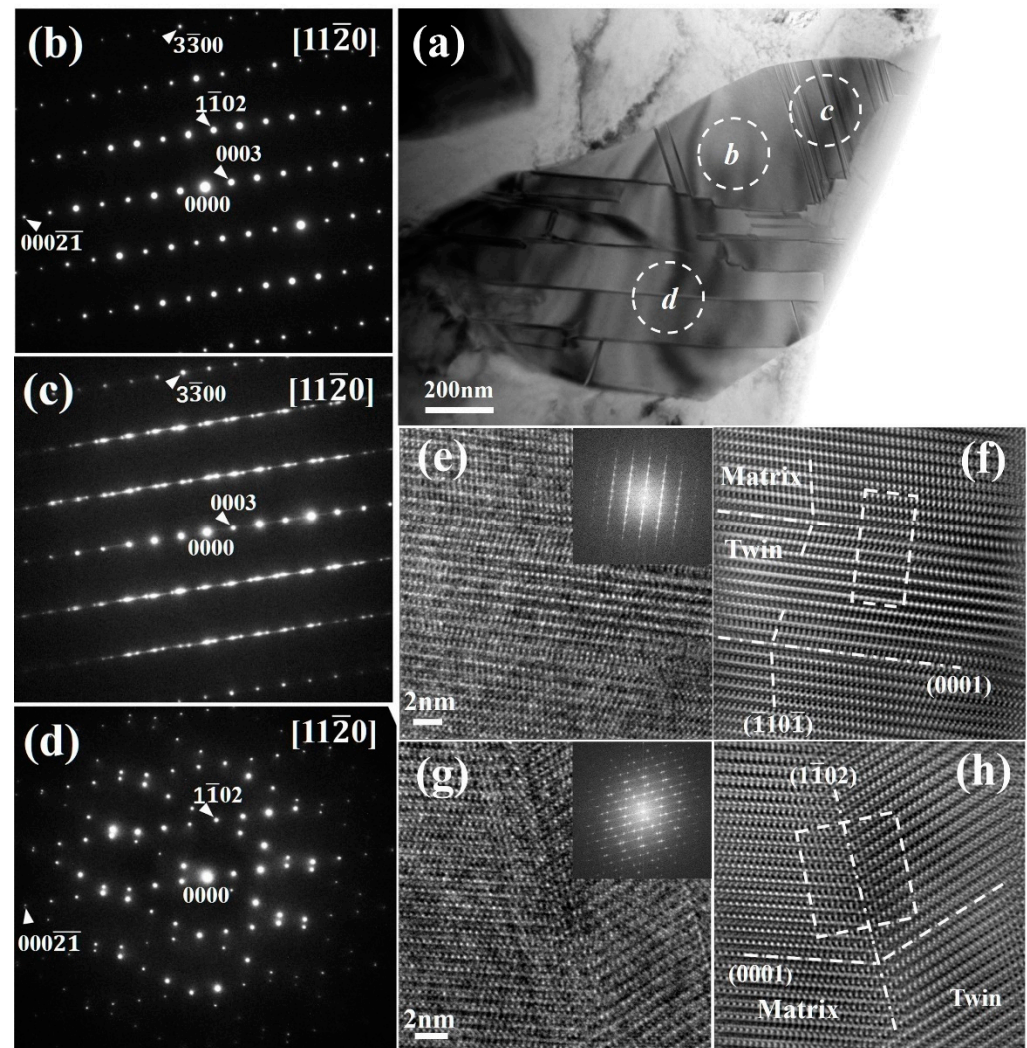

Figure 3. (**a**) A bright-field TEM image of the μ phase with twins contrast; (**b**–**d**) corresponding SAED patterns from the circled regions "*b*", "*c*", and "*d*" in (**a**), respectively; (**e**) and (**g**) high-resolution TEM images of $(0001)_\mu$ and $(102)_\mu$ twins along $[11\bar{2}0]_\mu$ ZA, and the corresponding FFT patterns are displayed in the upper right corner, whereas (**f**) and (**h**) present the inverse FFT lattice images of (**e**) and (**g**), respectively.

There are two sets of parallel lines shown in one μ phase particle (Figure 3a). One set is close to the horizontal direction (marked as the "*d*" region), whereas the other possesses a small angle with the vertical direction (marked as "*c*" region). Figure 3b–d present corresponding SAED patterns along $[11\bar{2}0]$ zone axis (ZA) of regions "*b*", "*c*", and "*d*" in Figure 3a. As shown in Figure 3c,d, one can find that two twin substructures could be indexed in the μ phase, i.e., $(0001)_\mu$ and $(1\bar{1}02)_\mu$ twins. The $(0001)_\mu$ twins are several or dozens of nanometers in width with high density (Figure 3e), while $(1\bar{1}02)_\mu$ twins are about

200 nm in width (Figure 3a). The $(0001)_\mu$ twins are more common than $(1\bar{1}02)_\mu$ twins in the specimen. To obtain further information on these two types of twins, high-resolution TEM (HRTEM) images are shown in Figure 3e,g. The corresponding Fourier-filtered transformed (FFT) diffraction patterns of Figure 3e,g are shown in the top right corner, the same as Figure 3c,d. Figure 3f,h present the inversed FFT lattice images of Figure 3e,g, respectively. In Figure 3f, the dashed-dotted and dashed lines indicate $(0001)_\mu$ and $(\bar{1}101)_\mu$ lattice planes, respectively. And, the dashed-dotted and dashed lines in Figure 3i indicate the $(1\bar{1}02)_\mu$ and $(0001)_\mu$ lattice planes, respectively.

3.2. Basal Defects and $(0001)_\mu$ Twin Substructure

The $(0001)_\mu$ planar defects in the μ phase are always observed in the present study, which can induce lamellar contrasts compared to the perfect μ phase by forming SFs and twins. The $(0001)_\mu$ plane is the close-packed and slip plane of the μ structure [30,31]. SFs can be produced on the $(0001)_\mu$ planes by the emission of partial dislocations. The $(0001)_\mu$ twins can easily form due to consecutive basal planar SFs by synchro-shear inside Laves triple-layers [28,30], as discussed earlier by Ma et al. and Carvalho et al. [26,29]. To provide fundamental insights into the formation of $(0001)_\mu$ twins, a schematic diagram of the formation process is shown in Figure 4. Figure 4a shows the perfect lattice illustration of the μ phase along $[11\bar{2}0]_\mu$ ZA projection and the construction units of Zr_4Al_3 and $MgCu_2$-type lattices are superimposed alternately along the $(0001)_\mu$ planes. The atoms occupying different positions are represented by different colors (red and blue spheres). Figure 4b,c shows the formation process of $(0001)_\mu$ twins in the μ phase. The $1/6\,[\bar{1}100]_\mu$ (about 0.138 nm) partial dislocation glided into the $MgCu_2$-type lattice and left a SF (Figure 4b). In the case of two successive SFs in one MgCu2-type lattice (as shown in Figure 4b,c), $(0001)_\mu$ twins form in the μ phase (Figure 4c). If the basal slip occurs in two adjacent $MgCu_2$ units (as shown in Figure 4e), $(0001)_\mu$ twins are thickened. Atomic configurations of $(0001)_\mu$ twins in the μ phase are further investigated by ACTEM in Figure 4d,f, which are consistent with the diagrams shown in Figure 4c,e, respectively.
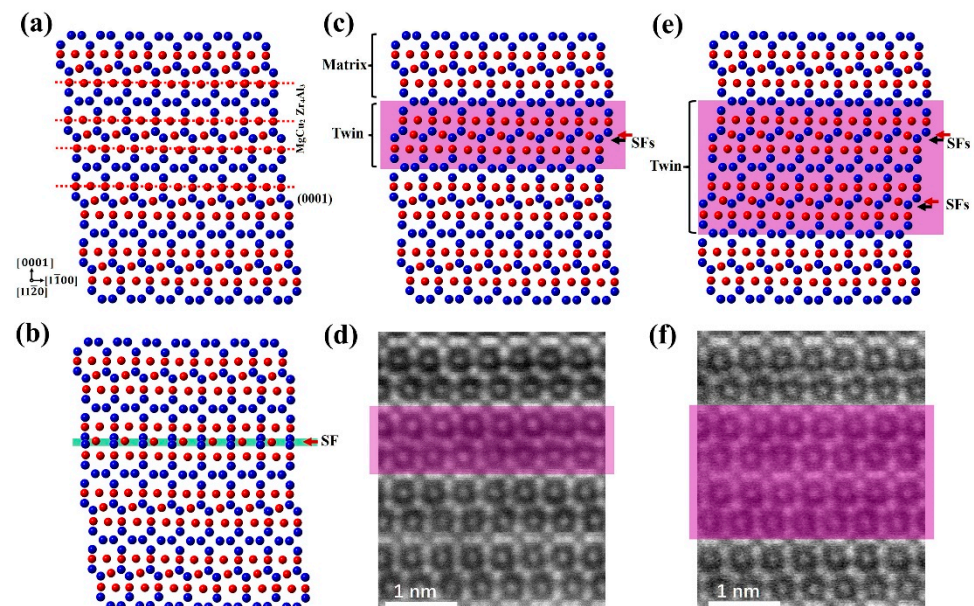

Figure 4. (**a**) The atomic arrangement of a perfect crystal lattice of the μ phase, showing alternating stacking of Zr_4Al_3 and $MgCu_2$ units along $[11\bar{2}0]_\mu$ ZA, (**b**) one stacking fault (SF, red spheres) on (0001) planes in $MgCu_2$-type unit of the μ phase, and the red arrow means the slip direction of the partial dislocation and a layer SF, (**c,d**) atomic arrangement diagram and STEM image of (0001) twins in the μ phase, and (**e,f**) atomic arrangement diagram and STEM image of the growth of (0001) twins. Red-colored spheres mean Fe/Ni atoms, and blue-colored spheres mean W/Mo atoms.

3.3. Pyramidal Defects and $(1\bar{1}02)_\mu$ Twin Substructure

The activity of non-basal slip systems makes an important contribution to the ductility of hexagonal crystals and is the main contributor for the deformation along the *c*-axis [28]. Besides the $(0001)_\mu$ basal plane slip, $(\bar{1}101)_\mu$ and $(1\bar{1}02)_\mu$ pyramidal planar slips are other forms to adapt to deformation [26,28,29]. The dislocations can slip from the matrix into non-basal slip systems of μ phase during deformation. Shear deformation of non-basal planes is associated with long-range diffusion or local atomic rearrangement [26,28,29].

As shown in Figure 3, $(1\bar{1}02)_\mu$ twins can be observed with $(0001)_\mu$ twins. Though $(1\bar{1}02)_\mu$ twins in the μ phase have been reported by several researchers [26,28,29], the twinning mechanism still needs further exploration. Figure 5 presents the possible $(1\bar{1}02)_\mu$ twinning mechanism in the μ phase. Figure 5a presents the atomic arrangement diagram of the μ phase along $[11\bar{2}0]_\mu$ ZA, where the red-colored rectangular and quadrilateral frames represent the periodic units of Zr_4Al_3- and $MgCu_2$-type lattices, respectively. The detailed twinning process is shown in Figure 5b. The periodic units of μ phase can be easily represented as a combination of rectangular and quadrilateral structures. The μ unit rotates, and the arrangement of rectangular and quadrilateral structures is exchanged under the influence of shear strain on the $(1\bar{1}02)_\mu$ pyramidal plane (Figure 5(b1)). The atoms (red-colored spheres near the red arrow) move about $1/12 [1\bar{1}01]_\mu$ in the shear direction (Figure 5(b1)). During the transition from the quadrilateral structure to rectangular structure (Figure 5(b2)), three atoms inside the quadrilateral structure are rearranged and the atom in the middle of the upper sideline (red-colored sphere) are moved into this structure (Figure 5(b3)). The number of atoms inside the structure increased from 3 to 4, and these atoms form a rectangle-shaped arrangement (Figure 5(b3). During the transition from rectangular to quadrilateral structure, the movement of atoms occurs in an opposite process. During the shear process, one layer of $(1\bar{1}02)_\mu$ planar faults is formed, which has a twin symmetrical relationship with the original lattice about the $(1\bar{1}02)_\mu$ plane overlays a translation vector $1/6 [1\bar{1}01]_\mu$ (Figure 5(b4)). If the planar faults expand continuously, $(1\bar{1}02)_\mu$ twins are formed with a $1/6 [1\bar{1}01]_\mu$ deviation between matrix and twin lattices (Figure 5(b5)). The deviation between matrix and twin lattices is reduced with $(1\bar{1}02)_\mu$ planar faults interval formation (Figure 5(b6)). Figure 5c presents the HRTEM image of $(1\bar{1}02)_\mu$ twins. The arrangement of atoms on both sides of the $(1\bar{1}02)_\mu$ twin boundary is consistent with the formation diagram in Figure 5(b5).

3.4. Influence of μ Phase on Shear Susceptibility

In general, the higher material strength implies that it is more prone to adiabatic shear failure, corresponding to higher adiabatic shear susceptibility [39,40]. In the past, precipitation-strengthening was used as an effective route for material strengthening [41,42]. Moreover, particle-reinforced composites have been widely developed and studied [35,43,44]. Experiments have shown that the shear susceptibility of alloys and composite materials depends on not only the volume fraction of particles but also their size, shape, and distribution [35,43,44]. Strain gradient theory and geometrically necessary dislocations provide a solid understanding of the formation behavior of shear bands [35,43,45].

In precipitation strengthening or particles-reinforced composites, the mechanical behavior is influenced by interfacial properties, i.e., coherent, or incoherent interfaces, and dislocation-interface interaction [46,47]. The existence of μ phase improves the strength of HEAs [25,33]. The size and distribution of μ phase can be changed after heat treatments [22,27], e.g., the μ phase grows after annealing at 1150 °C (Figure 1c,d). Therefore, controlling the content and distribution of the μ phase via heat treatment is an important strategy for regulating the strength and shear susceptibility of HEAs.
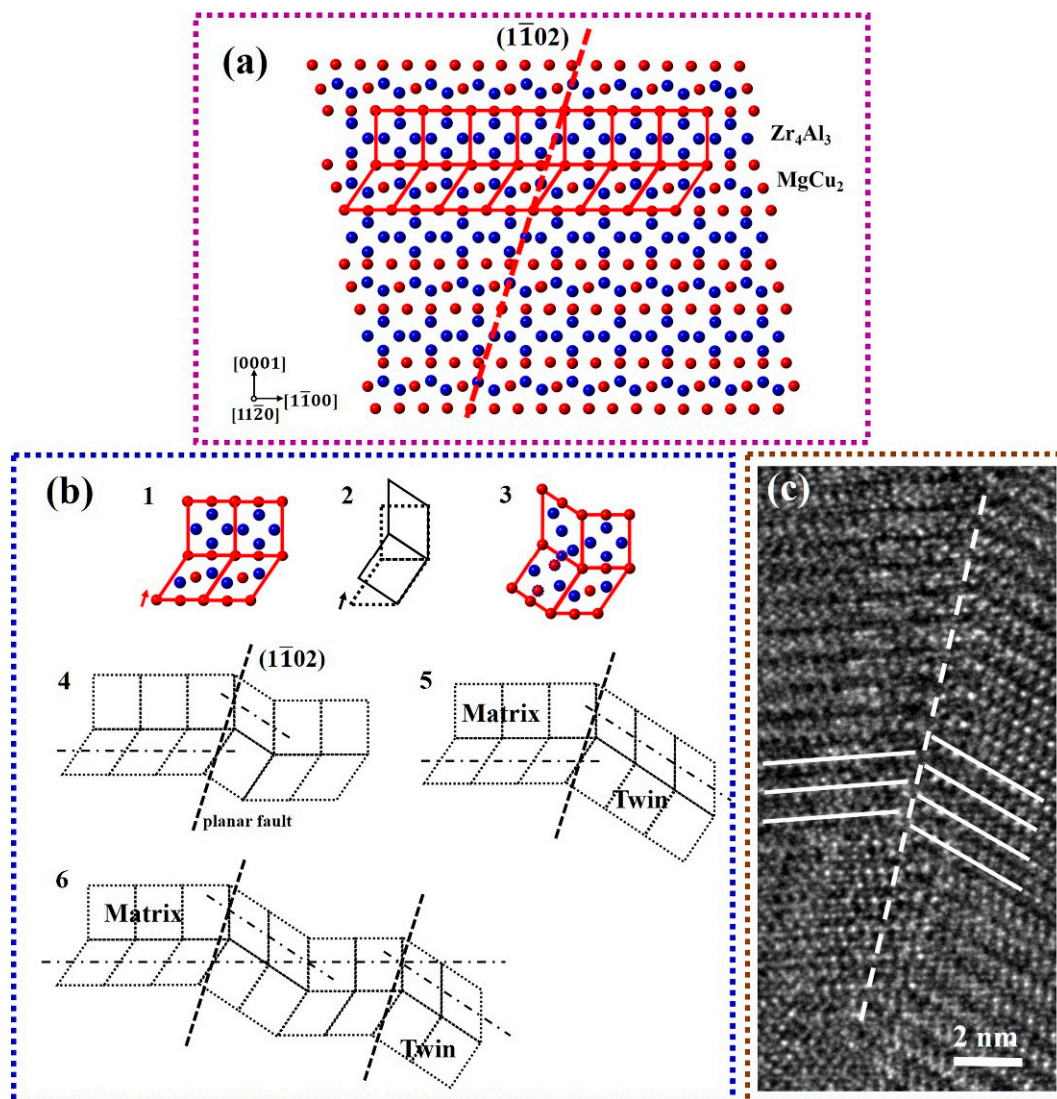
Figure 5. (**a**) The atomic arrangement of µ phase, consisting of rectangular (Zr_4Al_3) and quadrilateral ($MgCu_2$) structures as periodic units; (**b**) schematic illustration of $(1\bar{1}02)_\mu$ twinning mechanism in the µ phase, where red and black arrows in b1 and b2 show the shear direction; and (**c**) HRTEM image of $(1\bar{1}02)_\mu$ twins in the µ phase.

Coherent nano-scale precipitates can improve the strength without sacrificing plasticity [41,42]. In coherent systems, two phases exhibit a small lattice mismatch, i.e., atomic arrangement and slip systems are continuous across the interface [46,47], as shown in Figure 6a. The dislocations can cut the small particles through the coherent interface to maintain plasticity. With the growth of particles, the interface between particles and matrix can gradually lose its coherent characteristics [22,41]. As incoherent interfaces are opaque to dislocations, slip systems are not continuous (Figure 6(b2)). Hence, dislocations bypass and leave dislocation loops around the particles (Figure 6(b3)). The interface acts as dislocation sinks and a large number of dislocations accumulate at the interface during deformation. The strain gradient is induced by the formation of geometrically necessary dislocations (GNDs), rendering an impeding effect on dislocation movement (Figure 6(b4)). The high strain gradient is a strong driving force for the formation of adiabatic shear banding (Figure 6(b5,b6)) [33,36,48].
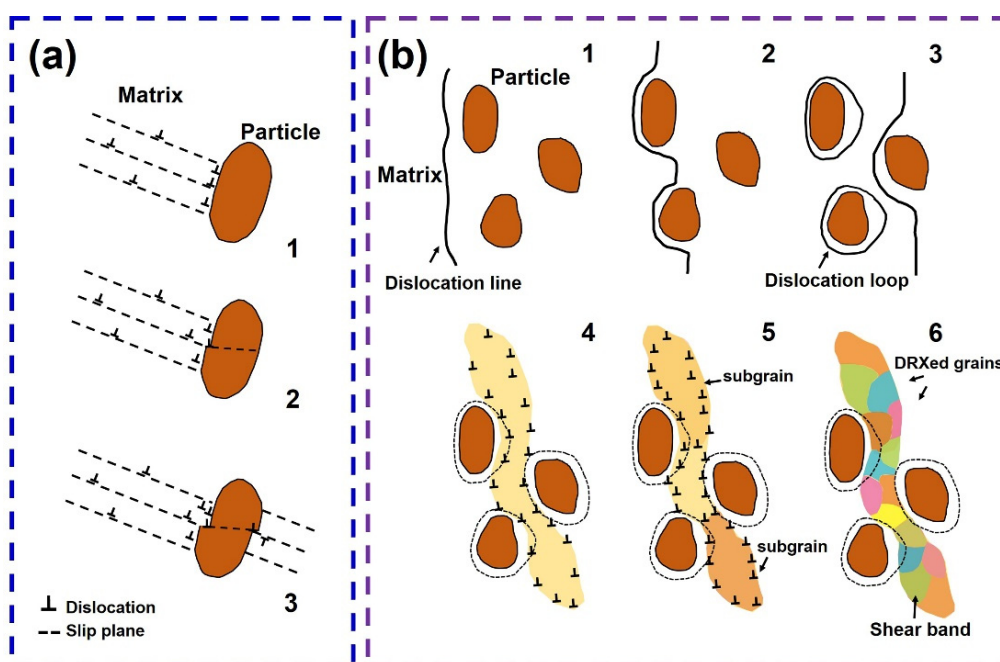
Figure 6. (**a**) Schematic diagram of dislocations cutting through the coherent nanoparticles, (**b1–b3**) Schematic diagram of dislocations bypassing incoherent μ phase particles, where dislocation loops are left around μ phase particles; (**b4**) dislocation accumulation at the particle boundaries and the formation of strain gradient due to GNDs; (**b5**) the continuous accumulation of dislocations, which divides the high strain gradient region into subgrains; and (**b6**) formation of DRXed grains accompanied with a reduction in dislocation density and occurrence of a shear band.

The μ phase possesses a complex structure and limited slip systems for the dislocation glide, and the multiple primary elements of μ phase in WHEA can have large elemental concentration fluctuations (Table 1). These improve the resistance of dislocation motion [49,50] through μ phase particles compared with the ordered FCC particles. The dislocations from the matrix interact with the μ phase and introduce basal and non-basal defects in μ particles [26,28,29]. Therefore, μ phase is easy to form twins on the $(0001)_\mu$ basal and $(1\bar{1}02)_\mu$ pyramidal planes. In addition, the formation of $(1\bar{1}02)_\mu$ twins is accompanied by atomic transportations and local atomic rearrangements. Hence, loads of twin substructures and pyramidal planar defects are formed in the μ phase, leading to a high strain hardening ability [25,51,52], which further aggravates the resistance of dislocation moving through μ phase particles. Owing to the high level of micro/nano-scale structural heterogeneities introduced by a large number of μ phase particles, the regions between particles form a high strain gradient accompanied by GNDs (Figure 6(b4)), which enhances the susceptibility of shear banding [33]. With the continuous accumulation of dislocations, the dislocations divide the high strain gradient regions into subgrains (Figure 6(b5)). Finally, with the further intensification of deformation, the dynamic recrystallization (DRX) grains [33,37] (equiaxed grains) are formed with the split of subgrains and crystal lattice rotation by dislocations accumulation (Figure 6(b6)). The regions between particles eventually combine with each other and form shear bands [33,48,53].

4. Conclusions

The μ phase, with twin substructures, in a multi-phase WMoFeNi HEA is investigated by SEM, XRD and TEM. This μ phase is dispersed in the FCC phase or located at the interface between FCC and BCC, which grows during annealing at 1150 °C for 24 h. The composition of μ phase is near-equiatomic to corresponding pure metallic elements, and the Fe/Ni and W/Mo elemental pairs are equivalent in the μ structure. The formation mechanism of $(0001)_\mu$ and $(1\bar{1}02)_\mu$ twins is investigated by ACTEM and geometric structural

analysis. The formation of $(1\bar{1}02)_\mu$ pyramidal planar faults involve atomic transportation and local atomic rearrangement. The basal $(0001)_\mu$ plane slip occurs more easily in the μ phase and the high-density $(0001)_\mu$ nano-twins are easier to form than the $(1\bar{1}02)_\mu$ twins. The high level of micro/nano-scale structural heterogeneities introduced by a large number of μ phase particles, the high strain gradient accompanied by geometrically necessary dislocations in the region between particles during deformation, and the high strength and strain hardening ability of μ phase with twin substructures could have important influences on shear susceptibility. This study provides novel insights into the design of self-sharpened HEAs.

Author Contributions: T.-W.L. and T.L. performed experiments, T.-W.L. conducted TEM observations, T.-W.L. and L.-H.D. designed, researched, and drafted the manuscript. All authors have read and agreed to the published version of the manuscript.

Conflicts of Interest: The authors declare no conflict of interest.

References

1. Wei, S.L.; Kim, S.J.; Kang, J.Y.; Zhang, Y.; Zhang, Y.; Furuhara, T.; Park, E.S.; Tasan, C.C. Natural-mixing guided design of refractory high-entropy alloys with as-cast tensile ductility. *Nat. Mater.* **2020**, *19*, 1175–1181. [CrossRef] [PubMed]
2. Snead, L.L.; Hoelzer, D.T.; Rieth, M.; Nemith, A. Refractory alloys: Vanadium, Niobium, Molybdenum, Tungsten. *Struct. Alloy. Nucl. Energy Appl.* **2019**, 585–640. [CrossRef]
3. Ren, C.; Fang, Z.Z.; Koopman, M.; Butler, B.; Paramore, J.; Middlemas, S. Methods for Improving Ductility of Tungsten-A Review. *Int. J. Refract. Met. Hard Mater.* **2018**, *75*, 170–183. [CrossRef]
4. Kim, D.K.; Lee, S.; Baek, W.H. Microstructural study of adiabatic shear bands formed by high-speed impact in a tungsten heavy alloy penetrator. *Mater. Sci. Eng. A* **1998**, *249*, 197–205. [CrossRef]
5. Kobayashi, S.; Hosoda, N.; Takashim, R. Tungsten alloys as radiation protection material. *Nucl. Instrum. Meth. A* **1997**, *390*, 426–430. [CrossRef]
6. Yeh, J.W.; Chen, S.K.; Lin, S.J.; Gan, J.Y.; Chin, T.S.; Shun, T.T. Nanostructured high-entropy alloys with Multiple principal elements: Novel alloy design concepts and outcomes. *Adv. Eng. Mater.* **2004**, *6*, 299–303. [CrossRef]
7. Cantor, B.; Chang, I.T.H.; Knight, P.; Vincent, A.J.B. Microstructural development in equiatomic multicomponent alloys. *Mater. Sci. Eng A* **2004**, *375–377*, 213–218. [CrossRef]
8. Zhang, Y.; Zuo, T.T.; Tang, Z.; Gao, M.C.; Dahmen, K.A.; Liaw, P.K.; Lu, Z.P. Microstructures and properties of high-entropy alloys. *Prog. Mater. Sci.* **2014**, *61*, 1–93. [CrossRef]
9. Li, Z.; Zhao, S.; Ritchie, R.O.; Meyers, M.A. Mechanical properties of high-entropy alloys with emphasis on face-centered cubic alloys. *Prog. Mater Sci.* **2019**, *102*, 296–345. [CrossRef]
10. George, E.P.; Raabe, D.; Ritchie, R.O. High-entropy alloys. *Nat. Rev. Mater.* **2019**, *4*, 515–534. [CrossRef]
11. Ye, Y.F.; Wang, Q.; Lu, J.; Liu, C.T.; Yang, Y. High-entropy alloy: Challenges and prospects. *Mater. Today* **2016**, *19*, 349–362. [CrossRef]
12. Bu, Y.Q.; Wang, H.T. Short-Range Order in Multicomponent Alloys. *Adv. Mech.* **2021**, *51*, 915–919.
13. Chen, J.; Liu, T.W.; Cao, F.H.; Wang, H.Y.; Chen, Y.; Dai, L.H. Deformation Behavior and Microstructure Evolution of CoCrNi Medium-Entropy Alloy Shaped Charge Liners. *Metals* **2022**, *12*, 811. [CrossRef]
14. Liu, F.; Liaw, P.K.; Zhang, Y. Recent Progress with BCC-Structured High-Entropy Alloys. *Metals* **2022**, *12*, 501. [CrossRef]
15. Yurchenko, N.; Panina, E.; Zherebtsov, S.; Stepanov, N. Design and characterization of eutectic refractory high entropy alloys. *Materialia* **2021**, *16*, 101057. [CrossRef]
16. Yurchenko, N.; Panina, E.; Rogal, Ł.; Shekhawat, L.; Zherebtsov, S.; Stepanov, N. Unique precipitations in a novel refractory Nb-Mo-Ti-Co high-entropy superalloy. *Mater. Res. Lett.* **2022**, *10*, 78–87. [CrossRef]
17. Senkov, O.N.; Wilks, G.B.; Miracle, D.B.; Chuang, C.P.; Liaw, P.K. Refractory high-entropy alloys. *Intermetallics* **2010**, *18*, 1758. [CrossRef]
18. Senkov, O.N.; Wilks, G.B.; Scott, J.M.; Miracle, D.B. Mechanical properties of Nb25Mo25Ta25W25 and V20Nb20Mo20Ta20W20 refractory high entropy alloys. *Intermetallics* **2011**, *19*, 698. [CrossRef]

19. Lee, W.H.; Park, K.B.; Yi, K.-W.; Lee, S.Y.; Park, K.; Lee, T.W.; Na, T.W.; Park, H.K. Synthesis of spherical V-Nb-Mo-Ta-W high-entropy alloy powder using hydrogen embrittlement and spheroidization by thermal plasma. *Metals* **2019**, *9*, 1296. [CrossRef]
20. Lu, S.; Li, X.; Liang, X.; Yang, W.; Chen, J. Effect of V and Ti on the Oxidation Resistance of WMoTaNb Refractory High-Entropy Alloy at High Temperature. *Metals* **2022**, *12*, 41. [CrossRef]
21. Seiser, B.; Drautz, R.; Pettifor, D.G. TCP phase predictions in Ni-based superalloys: Structure maps revisited. *Acta Mater.* **2011**, *59*, 749–763. [CrossRef]
22. Tian, S.; Wang, M.; Li, T.; Qian, B.; Xie, J. Influence of TCP phase and its morphology on creep properties of single crystal nickel-based superalloys. *Mater. Sci. Eng. A* **2010**, *527*, 5444–5451.
23. Calliari, I.; Pellizzari, M.; Zanellato, M.; Ramous, E. The phase stability in Cr–Ni and Cr–Mn duplex stainless steels. *J. Mater. Sci.* **2011**, *46*, 6916–6924. [CrossRef]
24. Liu, W.; Lu, Z.; He, J.; Luan, J.; Wang, Z.; Liu, B.; Liu, Y.; Chen, M.; Liu, C. Ductile CoCrFeNiMox high entropy alloys strengthened by hard intermetallic phases. *Acta Mater.* **2016**, *116*, 332–342. [CrossRef]
25. Wang, L.; Wang, L.; Tang, Y.C.; Luo, L.; Luo, L.S.; Su, Y.Q.; Guo, J.J.; Fu, H.Z. Microstructure and mechanical properties of CoCrFeNiWx high entropy alloys reinforced by μ phase particles. *J. Alloys Compd.* **2020**, *843*, 155997. [CrossRef]
26. Carvalho, P.; Haarsma, H.; Kooi, B.; Bronsveld, P.; Hosson, J.T.M. HRTEM study of Co7W6 and its typical defect structure. *Acta Mater.* **2000**, *48*, 2703–2712. [CrossRef]
27. Gao, S.; Liu, Z.Q.; Li, C.F.; Zhou, Y.Z.; Jin, T. In situ TEM investigation on the precipitation behavior of μ phase in Ni-base single crystal superalloys. *Acta Mater.* **2016**, *110*, 268–275. [CrossRef]
28. Cheng, Y.X.; Wang, G.L.; Liu, J.D.; He, L. Atomic configurations of planar defects in μ phase in Ni-based superalloys. *Scr. Mater.* **2021**, *193*, 27–32. [CrossRef]
29. Ma, S.; Li, X.; Zhang, J.; Liu, J.; Li, P.; Zhang, Y.; Jin, H.; Zhang, W.; Zhou, Y.; Sun, X.; et al. Atomic arrangement and formation of planar defects in the μ phase of Ni-base single crystal superalloys. *J. Alloys Compd.* **2018**, *766*, 775–783. [CrossRef]
30. Schröders, S.; Sandlöbes, S.; Berkels, B.; Korte-Kerzel, S. On the structure of defects in the Fe7Mo6 μ-Phase. *Acta Mater.* **2019**, *167*, 257–266. [CrossRef]
31. Schröders, S.; Sandlöbes, S.; Birke, C.; Loeck, M.; Peters, L.; Tromas, C.; Korte-Kerzel, S. Room temperature deformation in the Fe7Mo6 μ-Phase. *Int. J. Plast.* **2018**, *108*, 125–143. [CrossRef]
32. Zhang, Y.; Du, K.; Zhang, W.; Du, B.; Qi, D.; Li, W.; Song, M.; Sheng, L.; Ye, H. Shear deformation determined by short-range configuration of atoms in topologically close-packed crystal. *Acta Mater.* **2019**, *179*, 396–405. [CrossRef]
33. Liu, X.F.; Tian, Z.L.; Zhang, X.F.; Chen, H.H.; Liu, T.W.; Chen, Y.; Wang, Y.J.; Dai, L.H. "Self-sharpening" tungsten high-entropy alloy. *Acta Mater.* **2020**, *186*, 257–266. [CrossRef]
34. Li, Z.Z.; Zhao, S.T.; Wang, B.F.; Cui, S.; Chen, R.K.; Valiev, R.Z.; Meyers, M.A. The effects of ultra-fine-grained structure and cryogenic temperature on adiabatic shear localization in titanium. *Acta Mater.* **2019**, *181*, 408–422. [CrossRef]
35. Dai, L.H.; Ling, Z.; Bai, Y.L. A strain gradient-strengthening law for particle reinforced metal matrix composites. *Scr. Mater.* **1999**, *41*, 245–251. [CrossRef]
36. Dai, L.H.; Liu, L.F.; Bai, Y.L. Formation of adiabatic shear band in metal matrix composites. *Int. J. Solids Struct.* **2004**, *41*, 5979–5993. [CrossRef]
37. Rittel, D.; Landau, P.; Venkert, A. Dynamic recrystallization as a potential cause for adiabatic shear failure. *Phys. Rev. Lett.* **2008**, *101*, 165501. [CrossRef]
38. Yan, N.; Li, Z.; Xu, Y.; Meyers, M.A. Shear localization in metallic materials at high strain rates. *Prog. Mater. Sci.* **2021**, *119*, 100755. [CrossRef]
39. Dodd, B.; Bai, Y.L. *Adiabatic Shear Localization: Frontiers and Advances*; Pergamon Press: New York, NY, USA, 1992.
40. Wright, T.W. *The Physics and Mathematics of Adiabatic Shear Bands*; Cambridge University Press: Cambridge, UK, 2002.
41. Jang, T.J.; Choi, W.S.; Kim, D.W.; Choi, G.; Jun, H.; Ferrari, A.; Körmann, F.; Choi, P.P.; Sohn, S.S. Shear band-driven precipitate dispersion for ultrastrong ductile medium-entropy alloys. *Nat. Commun.* **2021**, *12*, 4703. [CrossRef]
42. Jiang, S.; Wang, H.; Wu, Y.; Liu, X.J.; Chen, H.H.; Yao, M.J.; Gault, B.; Ponge, D.; Raabe, D.; Hirata, A.; et al. Ultrastrong steel via minimal lattice misfit and high-density nanoprecipitation. *Nature* **2017**, *544*, 460–464. [CrossRef]
43. Xue, Z.; Huang, Y.; Li, M. Particle size effect inmetallic materials: A study by the theory of mechanism-based strain gradient plasticity. *Acta Mater.* **2002**, *50*, 149–160. [CrossRef]
44. Quested, T.E.; Greer, A.L. The effect of the size distribution of inoculant particles on as-cast grain size in aluminium alloys. *Acta Mater.* **2004**, *52*, 3859–3868. [CrossRef]
45. Gao, H.; Huang, Y.; Nix, W.D.; Hutchinson, J.W. Mechanism-based strain gradient plasticity-I. Theory. *J. Mech. Phys. Solids* **1999**, *47*, 1239–1263. [CrossRef]
46. Zhang, M.Y.; Wang, C.M.; Mi, G.Y.; Jiang, P.; Zhang, X.; Yan, X.H. Laser beam oscillation welded SiCp/2xx Al alloy: Microstructure, phase interface and mechanical properties. *Mater. Sci. Eng. A* **2021**, *820*, 141482. [CrossRef]
47. Zbib, H.M.; Overman, C.T.; Akasheh, F.; Bahr, D. Analysis of plastic deformation in nanoscale metallic multilayers with coherent and incoherent interfaces. *Int. J. Plast.* **2011**, *27*, 1618–1639. [CrossRef]
48. Tian, Z.L.; Wang, Y.J.; Chen, Y.; Dai, L.H. Strain gradient drives shear banding in metallic glasses. *Phys. Rev. B* **2017**, *96*, 094103. [CrossRef]
49. Ma, E. Unusual dislocation behavior in high-entropy alloys. *Scr. Mater.* **2020**, *181*, 127–133. [CrossRef]

50. Ding, Q.; Zhang, Y.; Chen, X.; Fu, X.; Chen, D.; Chen, S.; Gu, L.; Wei, F.; Bei, H.; Gao, Y.; et al. Tuning element distribution, structure and properties by composition in high-entropy alloys. *Nature* **2019**, *574*, 223–228. [CrossRef]
51. Ming, K.; Bi, X.; Wang, J. Precipitation strengthening of ductile $Cr_{15}Fe_{20}Co_{35}Ni_{20}Mo_{10}$ alloys. *Scr. Mater.* **2017**, *137*, 88–93. [CrossRef]
52. Liu, X.; Wu, Y.; Wang, Y.; Chen, J.; Bai, R.; Gao, L.; Xu, Z.; Wang, W.Y.; Tan, C.; Hui, X. Enhanced dynamic deformability and strengthening effect via twinning and microbanding in high density NiCoFeCrMoW high-entropy alloys. *J. Mater. Sci. Technol.* **2022**, *127*, 164–176. [CrossRef]
53. Fan, C.; Li, H.Q.; Kecskes, L.J.; Tao, K.X.; Choo, H.; Liaw, P.K.; Liu, C.T. Mechanical behavior of bulk amorphous alloys reinforced by ductile particles at cryogenic temperatures. *PRL* **2006**, *96*, 145506. [CrossRef] [PubMed]